Acoustic Levitation and Manipulation of Columns of Droplets with Integrated Optical Detection for Parallelisation of Reactions

Ruchi Gupta[*,1], Nicholas J. Goddard*[2]

[1] School of Chemistry, University of Birmingham, Birmingham, B15 2TT, UK

[2] Process Instruments, Turf Street, Burnley, Lancashire, BB11 3BP, UK

*Corresponding author: r.gupta.3@bham.ac.uk

Supplementary Information

Instrumentation

The electronics for the acoustic levitation system comprised of two printed circuit boards (PCB). The first board (USB Master) took data from a computer and distributed this data to up to twelve tile boards each of which could accommodate 64 ultrasonic transducers arranged in an 8 by 8 square array at 10 mm pitch. As shown in Figure S1, the USB Master board had a USB3.0 interface using an FT601Q USB to 32-bit first-in, first-out (FIFO) bridge chip (Future Technology Devices International Ltd, Glasgow, UK) which passed data to a T20Q144 field programmable gate array (FPGA) (Efinix Inc., Cupertino, USA). The data from the USB interface was stored in a dual-port RAM in the FPGA and read out at the required rate from the other port of the dual port RAM. The data read from the dual port RAM was then passed to 768 6-bit phase generators, giving a phase resolution of π/32. The output of the phase generators was then serialised along with control information and output as four 18-bit serial data streams running at 46.08 MHz (40 kHz transducer frequency × 64 possible phases × 18 bits). The output of the FPGA could control up to 12 low-voltage differential signalling (LVDS) drivers with each obtaining 4-bits of data, a 46.08 MHz clock, and a 2.56 MHz synchronising (sync) signal. Each LVDS driver output 12-bits with 8-bits for differential data, 2-bits for differential clock, and 2-bits for differential sync signal.

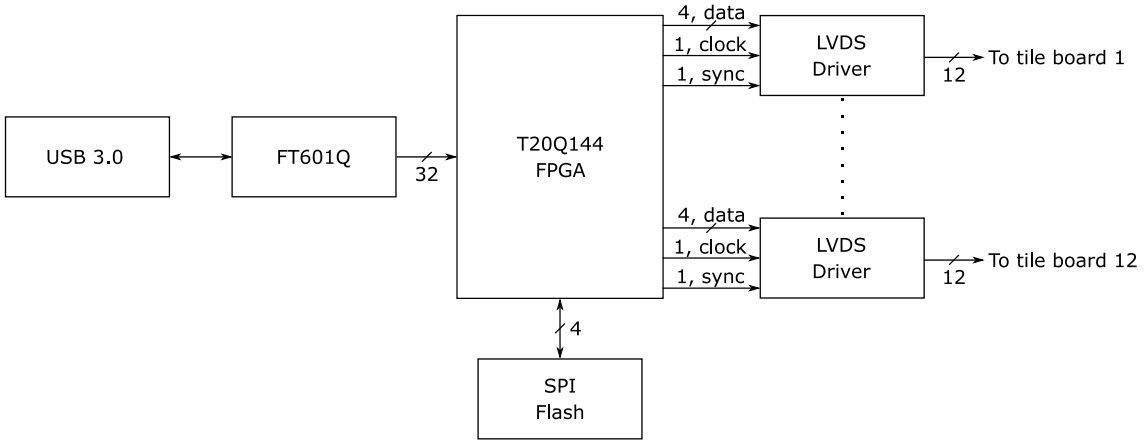

Figure S1: Block diagram of the electronics on the USB Master

Each LVDS driver sent the information to the corresponding LVDS receiver on each tile board over a 100 Ω twisted-pair ribbon cable. Because all tile boards were driven from the same USB Master, they were all perfectly synchronised. The USB3 FIFO interface on the USB Master board was clocked at 66.67 MHz and provided 4 bytes of data (32 bits) per clock cycle, giving a data transfer rate of 266.67 Mbytes per second. This meant that the entire 768 bytes for all 12 tile boards could be transmitted in 2.88 µs, which was less than the cycle time (25 µs) of the 40 kHz ultrasonic transducers.

As shown in Figure S2, the LVDS receiver de-serialised the data using four 18-bit shift registers. Sixty-four of the shift register outputs contained the phase information used to drive the transducers *via* Toshiba TC78H620FNG dual H-bridge drivers. Of the remaining 8 bits, one bit was used to globally enable the H-bridge drivers, one bit to enable the on-board step-down power supply (AP63300 buck converter chip, Diodes Inc., Plano, USA) and the remaining 6-bits were used to set the voltage applied to the ultrasonic transducers. The step-down power supply was controlled by an 8-bit digital-to-analogue converter (DAC, AD5330BRUZ, Analog Devices Inc., Massachusetts, USA). The step-down power supply could provide up to 3 A output current at between 3 and 9 V. Because the MA40S4S ultrasonic transducers have a maximum voltage rating of 20 V p-p, as noted above the power supply was limited to 9 V maximum giving at most 18 V p-p at the transducers.

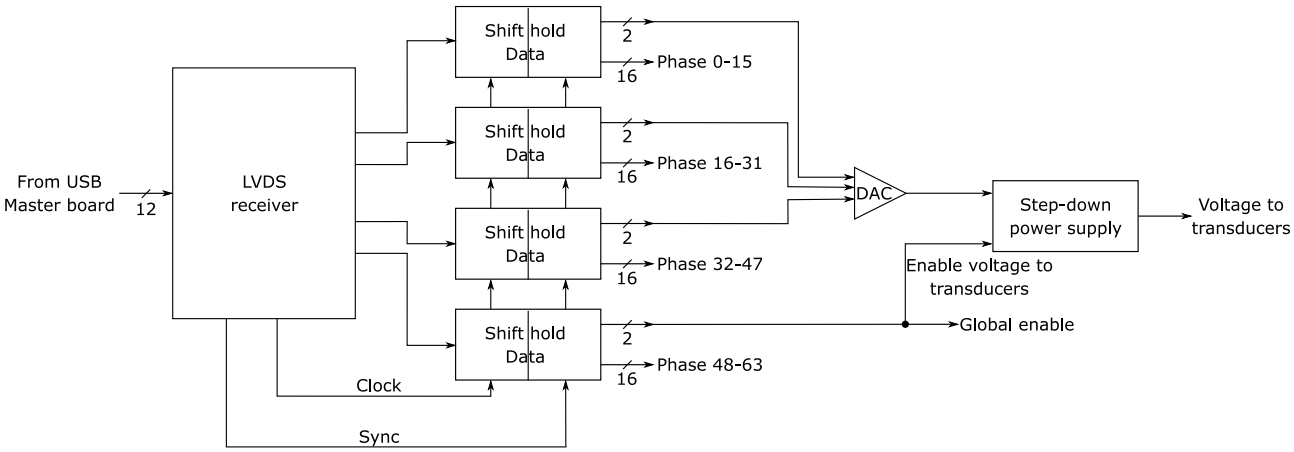

Figure S2: Block diagram of the electronics on each tile board

USB Master software: Code for the FPGA on the USB Master board was written in Verilog and compiled into a bitstream using Efinix Inc.'s Efinity software. Once debugged, the resulting bitstream was written to the on-board serial peripheral interface (SPI) flash chips on the USB Master board. To control the USB Master board using a computer, a software was written in C++ and compiled using C++Builder version 10.4 (Embarcadero Technologies Inc., Austin, USA). The software had a graphical user interface (GUI, see Figure S3) that allowed the phase of each transducer to be controlled either manually or programmatically. For programmatic control, csv files containing x-, y-

and z-coordinates of foci were read into the GUI and converted to phases using either iterative backpropagation (IBP) or checkerboard algorithms. The phases were updated as foci changed in time. The total number of steps (N) taken to travel from start to end as well as the time interval (Δt) between consecutive steps were set in the GUI. The voltage used to drive the transducers was controlled at the tile board level, but selected transducers could be enabled/disabled.

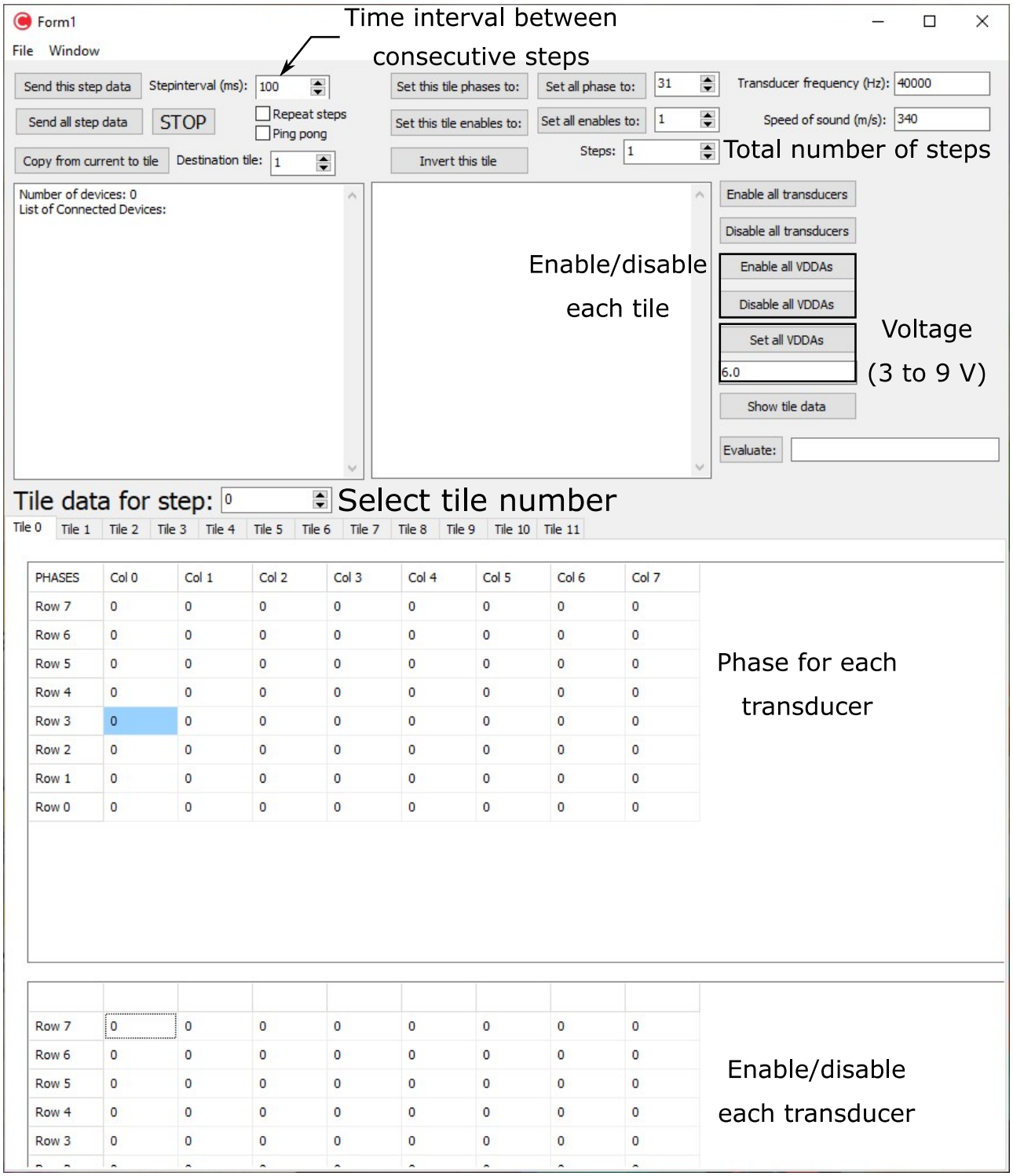

Figure S3: Screenshot of the GUI of our USB Master software

Simulation software: To visualise acoustic pressure (P), Gor'kov potential (U), and acoustic force (F^{ARF}), we wrote a simulation program in C++. The software read csv files containing x-, y- and z-coordinates of transducers, their normal vectors, phases, applied voltage, and pressure factor. P at each point in space was calculated by taking an algebraic sum of acoustic pressure produced by the jth transducer (see Equation S1).

$$P = \sum_{j=1}^{n} P_j \qquad \text{Equation S1}$$

And,

$$P_j = 2\frac{P_0}{d_j} cos\left(\frac{2\pi}{\lambda} d_j + \varphi_j\right) \frac{J_1\left(\frac{2\pi r sin\theta_j}{\lambda}\right)}{\frac{2\pi r sin\theta_j}{\lambda}} \qquad \text{Equation S2}$$

Where, P_0 is the pressure rating of transducers given in Pa·m (0.17), λ is wavelength of sound (~8.65 mm), d_j is the distance between the centre of the jth transducer and a point in space, φ_j is the phase of the jth transducer, J_1 is first order Bessel function, r is the inner radius of the transducers (~4 mm), and θ_j is angle between the normal of the jth transducer and a line joining the centre of the jth transducer to a point in space. The Gor'kov potential (U) and acoustic force (F^{ARF}) are given by Equations S3 and S4, respectively.

$$U = K_1|P|^2 - K_2\left(|P_x|^2 + |P_y|^2 + |P_z|^2\right) \qquad \text{Equation S3}$$

And,

$$K_1 = \frac{V}{4}\left(\frac{1}{\rho_0 {c_0}^2} - \frac{1}{\rho_p {c_p}^2}\right) \quad \text{and} \quad K_2 = \frac{3V}{4}\left(\frac{\rho_0 - \rho_p}{(2\pi f)^2 \rho_0 (\rho_0 + 2\rho_p)}\right)$$

$$F^{ARF} = -\nabla U \qquad \text{Equation S4}$$

Where, P_x, P_y and P_z are partial derivates of acoustic pressure with respect to x, y, and z, respectively. V is object volume, f is frequency of sound waves (40 kHz), ρ is density and c is speed of sound with subscripts o and p referring to air and object, respectively.

Phase calculation using the checkerboard algorithm: For creating a single focus at $[x_p(t), y_p(t), z_p(t)]$, the phase ($\varphi_j(t)$) of the jth transducer located at $[x_j, y_j, z_j]$ at any time can be calculated using Equation

S5. For creating two foci, alternate transducers in the acoustic levitator were assigned to one of the two foci and then Equation S5 was used to calculate phases.

$$\varphi_j(t) = \frac{2\pi c_o}{f}\sqrt{(x_j - x_p(t))^2 + (y_j - y_p(t))^2 + (z_j - z_p(t))^2} \qquad \text{Equation S5}$$

Fluorescence intensity of levitated droplets: A plot of gray scale value along the major axis of a levitated droplet is shown in Figure S4. Figure S4 clearly shows that the light source generates bright spots at the edges of the droplets. In addition, the droplet acts as a lens, focusing the impinging light within the droplet. This is then reflected back from the other end of the droplet, which causes bright spots within the droplet that can saturate the camera at higher fluorescein concentrations. This raises challenges in image processing to remove these artefacts. The method employed was to use ImageJ to threshold the images, followed by extraction of the centroid of the droplet. Because the bright spots appeared at the edges of the droplet or within the droplet close to the edge furthest from the light source, from the centroid it was possible to determine a location within the droplet where there were no bright spots. The average intensity in a square region around this location was then extracted and used to generate calibration curves and from these the concentration of fluorescein generated by esterase in the merged droplets.

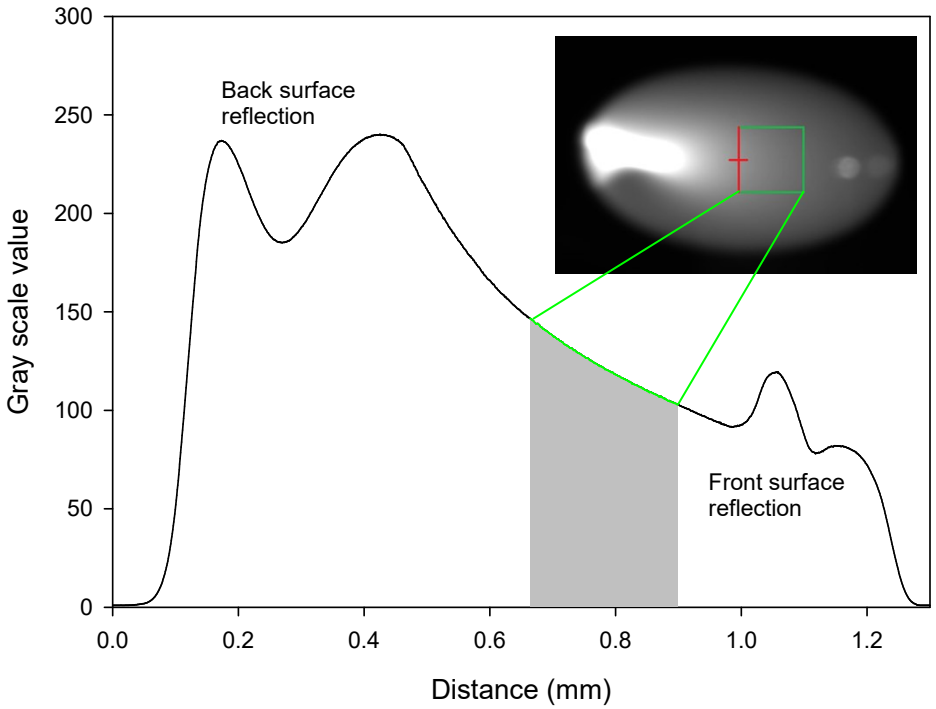

Figure S4: Gray scale value distribution inside a levitated droplet where the grey area shows the portion of the droplet used to determine mean fluorescence intensity of the droplet

One focus and two foci: Figure S5 plots P^2 in the xz-plane at x=0 in for a single focus at [0, 0, 0] and two foci at [-20, 0, 0] and [20, 0, 0] obtained using our simulation software and phases generated by the checkerboard algorithm.

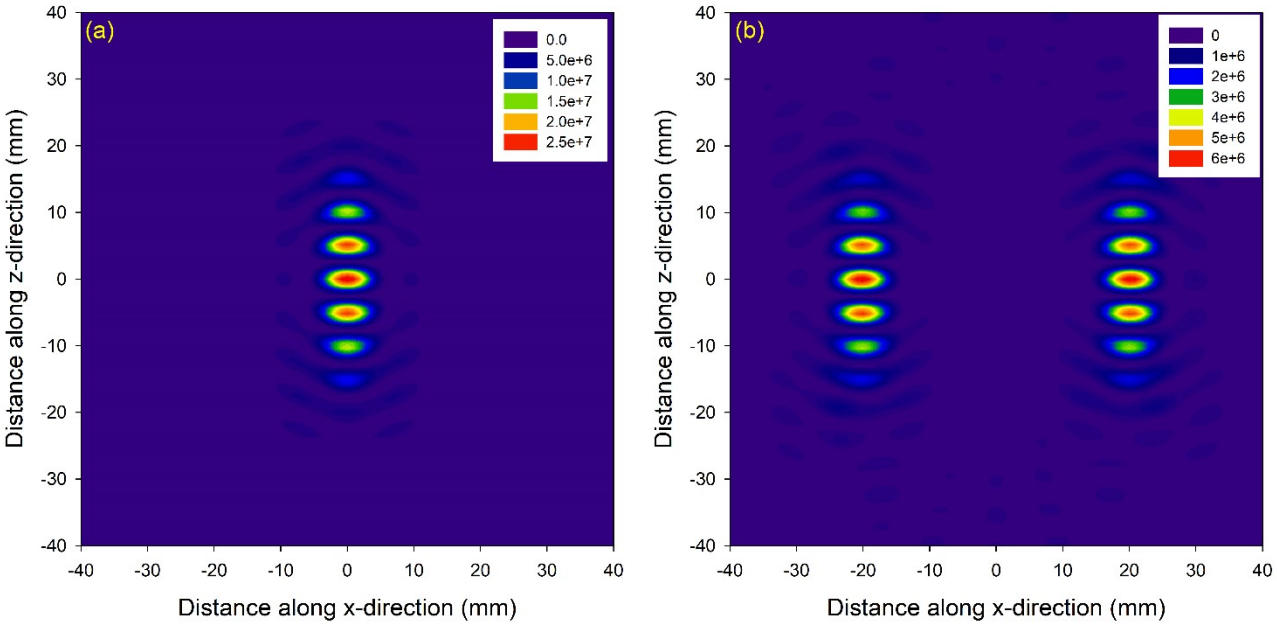

Figure S5: Distribution of P^2 determined using our simulation software in case of (a) a single focal point and (b) two focal points

Size of levitated droplets: Droplets of different volumes were levitated in traps at a single focus and two foci. Levitated droplets had an oblate spheroid shape and a plot of their minor and major axes dimensions as a function of their volume is provided in Figure S6. Because of the acoustic pressure difference in the z dimension, the height of the droplets changes significantly less than the width as the droplet volume increases.

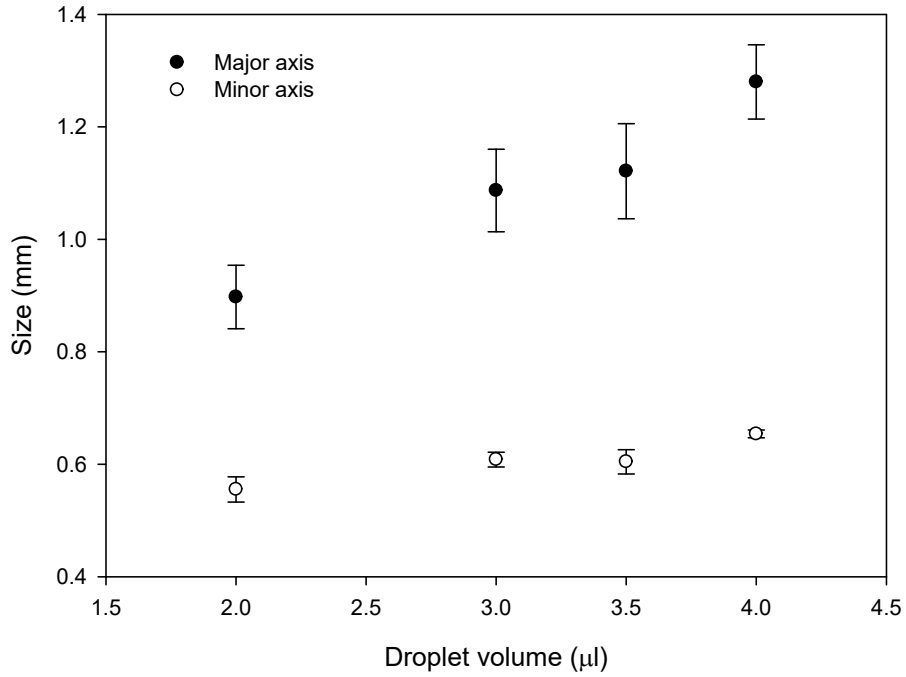

Figure S6: Plot of dimensions of minor and major axes of levitated droplets of different volumes where the minor and major axes align with the z- and x-directions, respectively

Temperature measurement of levitated droplets: We levitated a line of 3 droplets at a single focus and captured FLIR images for 11 min after every 1 min. Figure S7 shows a complete FLIR image taken at 11 minutes after the introduction of the droplets. This image shows that the transducers were heating up to ~40 °C, which may explain the temperature rise observed in the droplets.

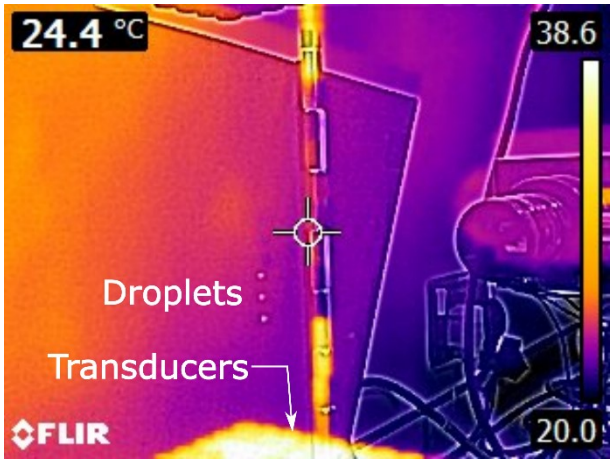

Figure S7: FLIR image showing the three levitated droplets and part of the lower transducer array

As shown in Figure S8, the temperature of levitated droplets increased by about 1.5 °C in 11 min and is slowly approaching a limiting value. It is unclear whether this temperature increase is a result of acoustic forces or convective heating from the transducers below the droplets.

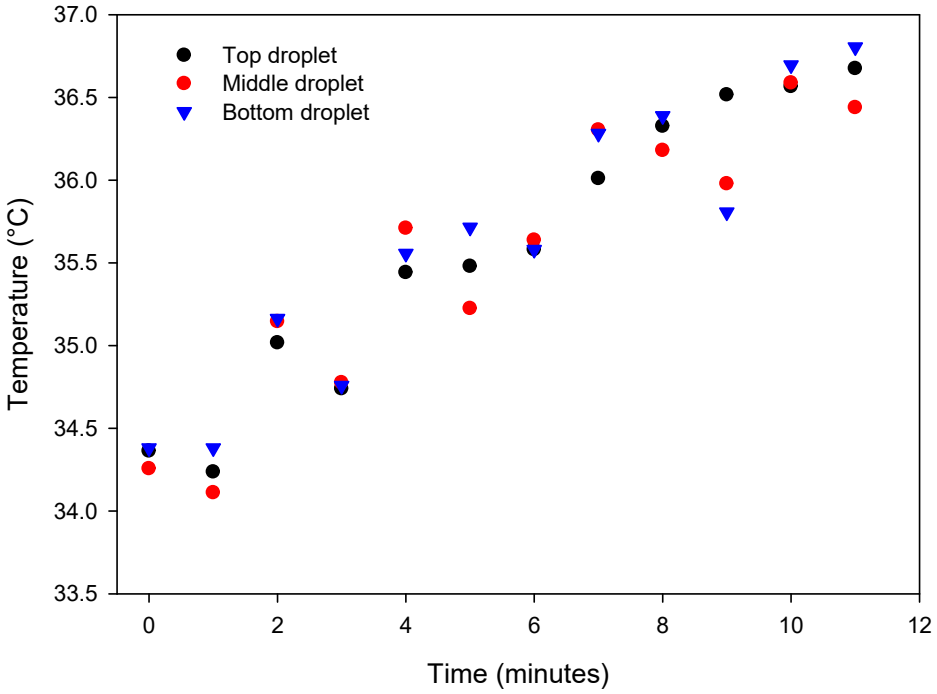

Figure S8: Temperature of a line of three droplets levitated at a single focal point with time

Comparison of IBP and checkerboard algorithms: To compare the two algorithms, we used them to calculate transducer phases for generating two foci at cartesian coordinates [-20, 0, 0] and [20, 0, 0] (both in mm). The two algorithms were then used to calculate transducer phases needed to move the two foci towards each other in a straight line along x-direction in the xz plane and merging them at [0, 0, 0]. Subsequently, we inputted the transducer phases generated by IBP and checkerboard algorithms in our simulation software to visualise the acoustic pressure distribution in the two cases (see Movies S1 and S2, respectively). The simulation of the IBP algorithm clearly shows sudden jumps in pressure distributions at 12.9, 21.2, 26.4 s and a final jump at 33.8 s when the foci merge. In contrast, the checkerboard algorithm gave much smoother transitions without jumps in pressure distributions.

To compare the two algorithms experimentally, lines of three expanded polystyrene (EPS) beads were levitated at each focus and their movements generated by IBP (Movie S3) and checkerboard (Movie S4) algorithms as the foci were merged were recorded. A comparison of Movies S3 and S4 shows that movements of levitated EPS beads in case of the IBP algorithm were more erratic than those generated by the checkerboard algorithm. Figures S9 (a) and (b) show erratic and smooth movements of EPS beads for IBP and checkerboard algorithms, respectively. In case of IBP algorithm, when the foci were about 10 mm apart as shown in Figure S9 (a), the levitated EPS beads stopped moving for a few seconds and then came in contact with each other all of a sudden. This sudden contact caused the EPS beads to spin around the merged foci. In contrast, the checkerboard algorithm resulted in

EPS beads to travel at about constant speed from start to end as well as much softer contact between the levitated beads when the foci merged.

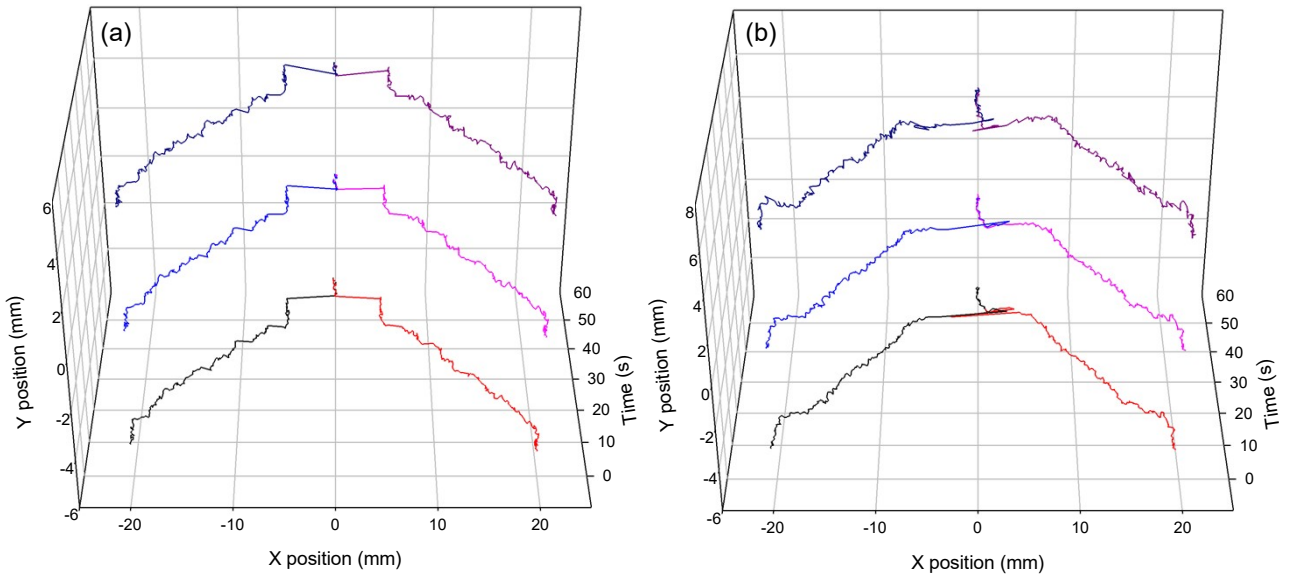

Figure S9: Paths of expanded polystyrene beads levitated at two foci that were merged using (a) iterative backpropagation (IBP) and (b) checkerboard algorithms

Subsequently, we levitated 4 µl droplet at each of the foci and tracked their movements generated by IBP and checkerboard algorithms as the focal were merged. A comparison of Movies S5 and S6 shows that droplet movements in case of the IBP algorithm were more erratic than those generated by the checkerboard algorithm, which is in line with our observations made with EPS beads. The erratic and smooth movements of droplets in case of IBP and checkerboard algorithms can also be seen in Figure S10 (a) and (b), respectively. Furthermore, Movies S5 and S6 show significant deformation of droplets when the foci were merged using the IBP than the checkerboard algorithm. Equally, the sudden contact between droplets when foci were merged using the IBP algorithm resulted in droplets to atomise much more often than on using the checkerboard algorithm. Thus, the checkerboard algorithm was used for all subsequent work.

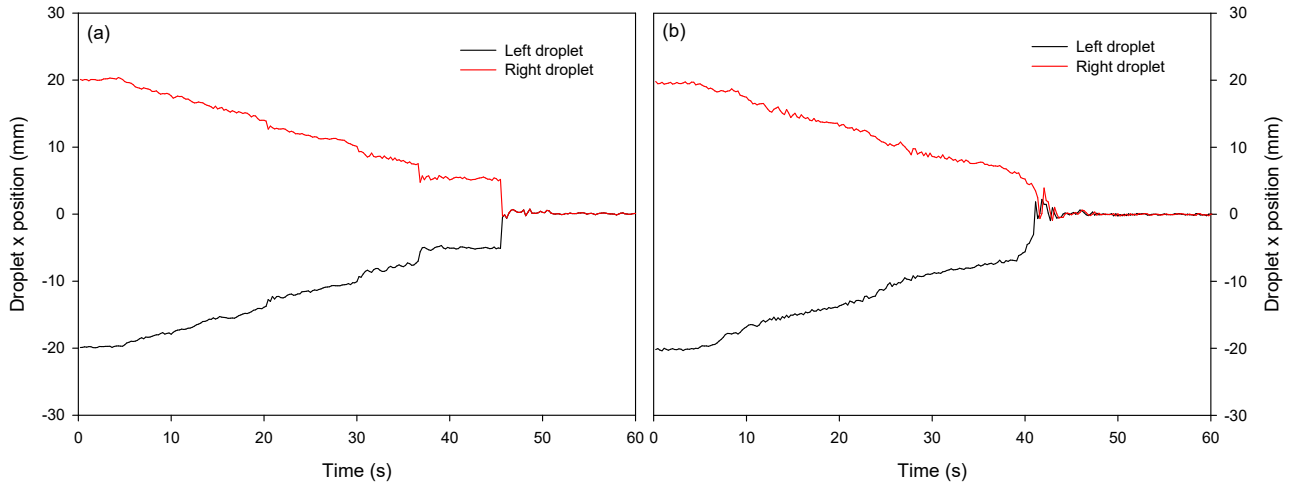

Figure S10: Paths of droplets levitated at two foci that were merged using (a) iterative backpropagation (IBP) and (b) checkerboard algorithms

Figure S11 gives a plot of P^2 as a function of z position at x = 0 (black trace) and ±20 mm (red trace) for a single trap and two traps, respectively generated using the IBP (Figure S11 (a)) and checkerboard (Figure S11 (b)) algorithms. The IBP algorithm gives similar P^2 for single trap but higher P^2 for two traps compared to the checkerboard algorithm.

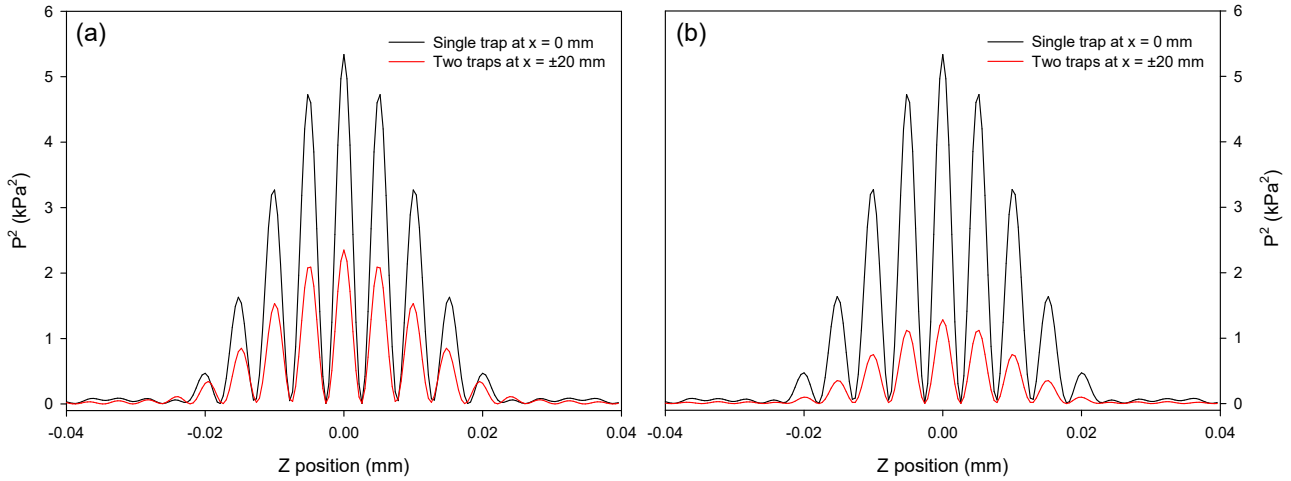

Figure S11: Distribution of P^2 along z at x=0 (black trace) and ±20 mm (red trace) generated using (a) the IBP and (b) the checkerboard algorithms and our simulation software for a single focus and two foci

Calibration curves of levitated fluorescein droplets: We pipetted a line of three 4 µl droplets of fluorescein in a single focus and captured images using the Daheng camera with a zoom lens. The process was repeated for droplets of different concentrations of fluorescein. The images were analysed and calibration curves for top, middle, and bottom droplets are provided in Figure S12. The

differences in intensities of the droplets are a result of non-uniformity of the beam from the blue LED.

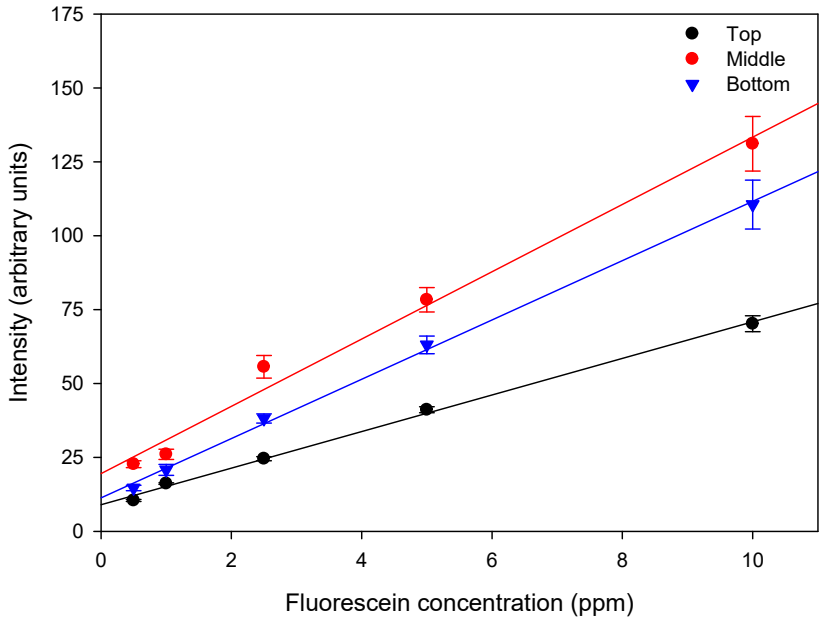

Figure S12: Calibration curves of three 4 µl fluorescein droplets levitated at a single focus at [0, 0, 0]

To gain confidence that our calibration curves can be used to estimate fluorescein concentrations of droplets, we merged buffer and 10 ppm fluorescein droplets. We then used the calibration curve to estimate fluorescein concentrations of the resulting merged droplets and compared with the expected concentrations. Figure S13 shows that the estimated fluorescein concentrations of top, middle and bottom droplets obtained by merging a buffer and 10 ppm fluorescein droplets is 5.91±0.31 ppm, 7.33±0.72 ppm and 5.24±0.31 ppm, respectively, which are close to the expected value of 5 ppm.

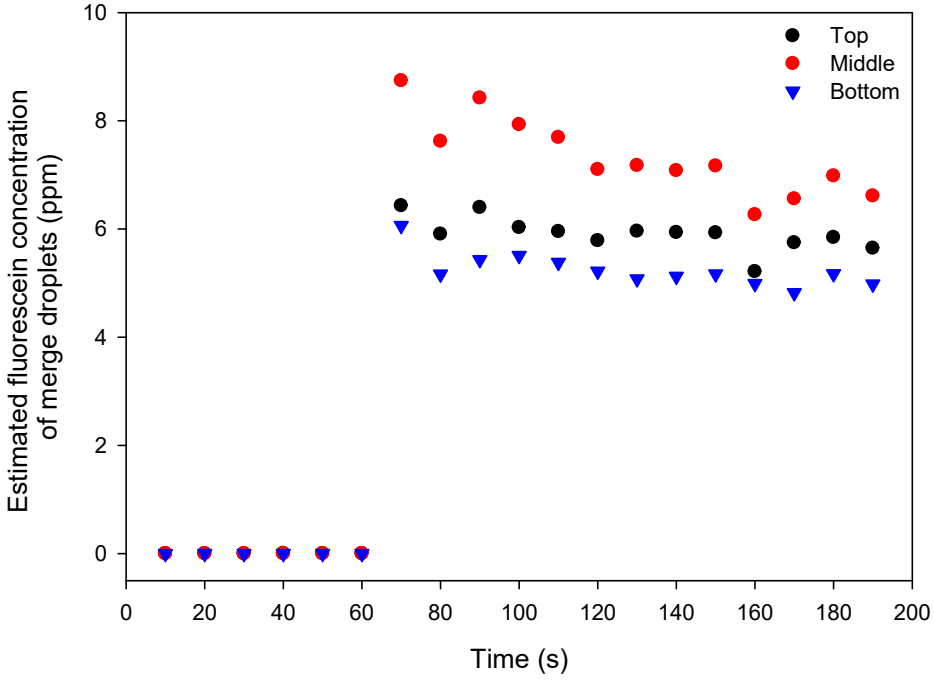

Figure S13: Estimated fluorescein concentration of droplets obtained by merging buffer and 10 ppm fluorescein droplets

Photobleaching and evaporation of levitated fluorescein droplets: We levitated three 10 ppm fluorescein droplets of 4 µl at a single focal position and captured images using the Daheng camera with a zoom lens after every 2 s for 180 s. The images were analysed and a plot of normalised intensity *versus* time for top, middle, and bottom droplets is provided in Figure S14. Figure S14 clearly shows that intensity of levitated 10 ppm fluorescein droplets decrease with time and was attributed to photobleaching caused by the intense blue LED light source used to illuminate levitated droplets. Furthermore, Figure S14 shows that the intensity of the middle droplet decayed at a faster rate than top and bottom droplets because the intensity of light sources was highest in the centre. As the intensity of droplets is decreasing with time, photobleaching is stronger than the increase in concentration of fluorescein caused by evaporation. We fitted the intensity *versus* time curves of 10 ppm fluorescein droplets to exponential decay with decay rates of 3.45×10^{-3} s^{-1} for top droplet, 6.35×10^{-3} s^{-1} for middle droplet, and 3.61×10^{-3} s^{-1} for bottom droplet.

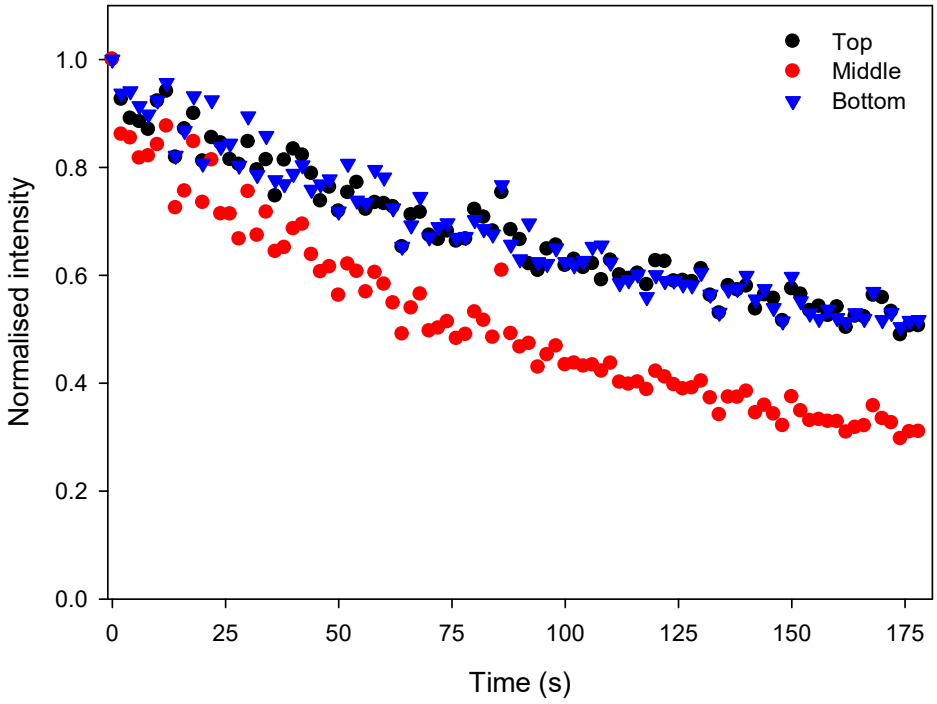

Figure S14: Normalised intensity *versus* time of 10 ppm fluorescein droplets levitated at a single focus

Enzyme assays: Plots of fluorescein concentrations without and with *versus* time for top droplets are shown in Figure S15. Similar plots for bottom droplets are shown in Figure S16.

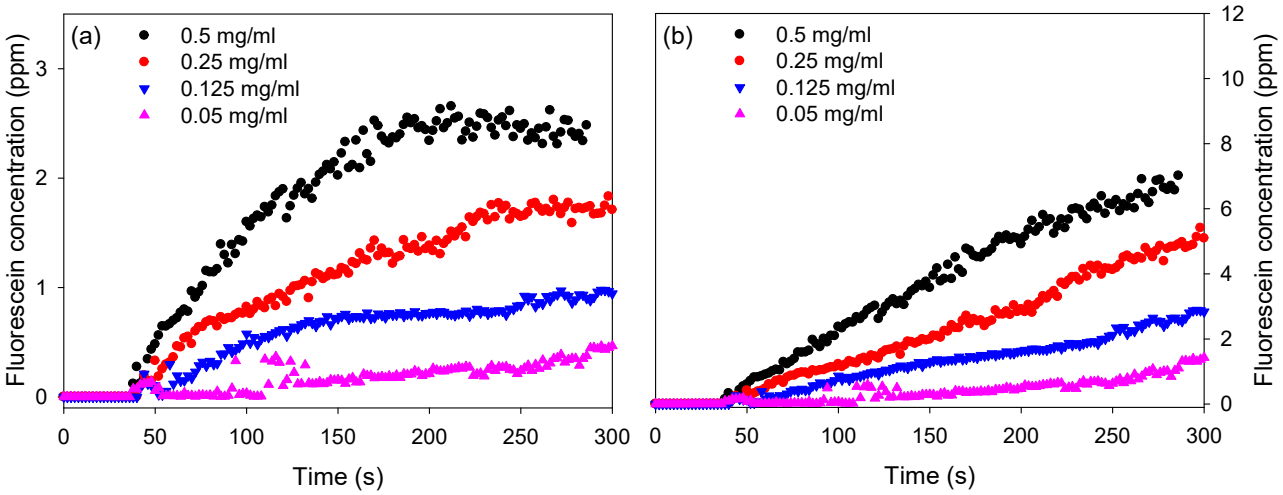

Figure S15: Fluorescein concentration *versus* time of a top droplet obtained by merging FDA and esterase enzyme (a) without and (b) with correction for photobleaching (legend provides enzyme concentration in the merged droplet and FDA concentration in the merged droplet was 25 ppm)

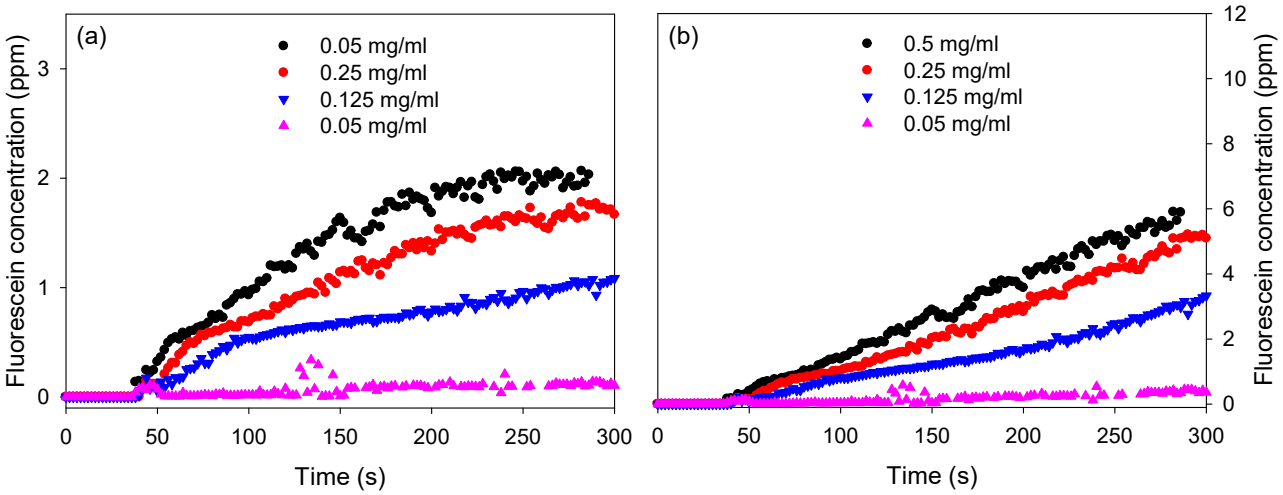

Figure S16: Fluorescein concentration *versus* time of a bottom droplet obtained by merging FDA and esterase enzyme (a) without and (b) with correction for photobleaching (legend provides enzyme concentration in the merged droplet and FDA concentration in the merged droplet was 25 ppm)